The role of accumulated plasticity on yield surface evolution

Knut Andreas Meyer[a,*], Johan Ahlström[b]

[a] *TU Braunschweig, Institute of Applied Mechanics, Germany*
[b] *Chalmers University of Technology, Department of Industrial and Materials Science, Division of Engineering Materials, Sweden*

Abstract

In this paper, we analyze one specific assumption used in many cyclic plasticity models: The dependence of the yield surface evolution on the accumulated plasticity, i.e. the time-integrated plastic multiplier. In carefully designed experiments, we measure this scalar variable and track the yield surface evolution. Our results show that this variable is insufficient to describe the isotropic or distortional hardening of the investigated steel, invalidating the commonly used assumption. The results highlight requirements for developing and verifying new isotropic and distortional hardening laws.

Keywords: Cyclic plasticity, isotropic hardening, distortional hardening, yield surface

1. Introduction

Modeling the plastic material response is necessary for accurate analyses in many industrial applications, such as sheet metal forming, rolling contact loading, and other applications where low cycle fatigue loading occur. Cyclic plasticity has, therefore, been a subject of intense research for many decades. Most cyclic plasticity models are extensions of the general framework presented in Chaboche (1986). In terms of isotropic hardening, however, the rule denoted "Classical isotropic hardening" is used by most authors. In these cases, the isotropic hardening evolution is only a function of the accumulated plasticity (See Section 3 for an exact definition). Some models, e.g. El Abdi et al. (1999); Zhou et al. (2018), include the so-called "strain-range memorization" effect introduced by Chaboche et al. (1979). This extension allows the saturated yield strength to depend on the plastic strain amplitude. In Chaboche (1986); Novak et al. (2019), approximate analyses based on peak stresses were conducted to show how the yield strength evolves due to the accumulated plasticity. In the present work, we explicitly measure the accumulated plasticity and then investigate how the yield strength evolves for a range of different loading conditions.

Between 1980 and 2000, both isotropic and kinematic hardening rules were researched intensively. However, in the same period, many experimental works showed that anisotropic yield surfaces evolve due to plastic deformations, cf. e.g. Ishikawa and Sasaki (1988). Bari and Hassan (2002) fitted the material response during non-proportional loading with advanced kinematic hardening laws. However, an anisotropic yield criteria is required to model some load cases. Many papers in the last decades have therefore considered distortional hardening, see e.g. Feigenbaum and Dafalias (2007); Harrysson and Ristinmaa (2007); Pietryga et al. (2012); Bartels and Mosler (2017). In their most basic form, these models include self- and cross-hardening. Many of these models predict that these hardening laws only depend on the accumulated plasticity during proportional loading. However, to the authors' knowledge, no study has been performed to validate this assumption. Hence, in the present work,

*Corresponding author
Email address: k.a.meyer@tu-bs.de (Knut Andreas Meyer)

we will also measure how the yield strength in a direction that is perpendicular to the loading evolves during cyclic loading.

The paper is organized as follows: Section 2 describes the material used for testing: the microstructure, heat treatment, and the tensile stress-strain curve. Section 3 introduces the material modeling framework we use to analyze the experiments. The specific experimental setup is described and motivated in Section 4. Finally, Section 5 presents the experimental results and discusses their implications for material modeling. For readability and simplicity, the major part of this paper considers a small strain framework. However, the experimental results are compensated such that the true stresses and strains are used. This compensation is outlined in Appendix A. Furthermore, a generalization of the analysis for a specific finite strain plasticity model is given in Appendix B.

2. Material

The material chosen for this study is pearlitic steel, a microstructure found in many industrial applications. Examples include railway rails and wheels, as well as high strength wires used as steel cords in tires and in ropes for suspension bridges. The pearlitic microstructure with its arrangement of alternating ferrite and cementite (Fe_3C) lamellas has a strong but saturating work hardening, cf. Taleff et al. (2002). In the present study, we start with seamless precision tubes of grade E-235 (EN10305-1 (2016)) with a 20 mm outer diameter and a 1.5 mm wall thickness. The next subsection describes the heat treatment procedure used to obtain a well-defined pearlitic microstructure. In Subsection 2.2, the overall stress-strain behavior of the normalized microstructure is discussed and compared to other materials.

2.1. Heat treatment

The goal of the heat treatment was to achieve an isotropic and homogeneous test material. In particular, the chemical composition, grain sizes, and lamellar spacing should have a low spatial variance. After cutting into 150 mm long pieces,

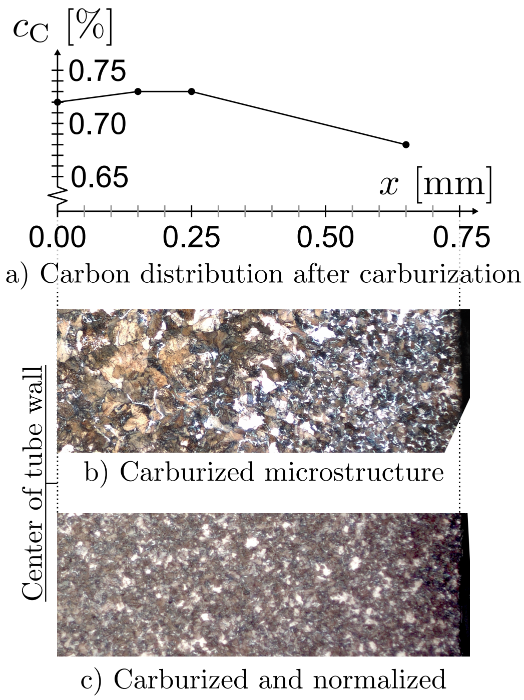

Figure 1: Carbon concentration and microstructure after heat treatments.

the tubes were carburized at 950°C for about eight hours and dwelled at 860°C for about three hours. During the carburization cycle, the carbon activity varied with time to acquire an even chemical composition throughout the wall thickness. A high initial carbon activity gave sufficient driving force to increase the carbon concentration at greater depths, while a lower activity in the next step ensured an even carbon level. Figure 1a shows that the resulting carbon levels were between 0.68 and 0.73 %. The average chemical composition is given in Table 1.

After carburization, the grain sizes were larger in the middle of the tube wall compared to at the surface, shown in Figure 1b. A subsequent normalization at 900 °C for 45 minutes in argon, followed by air cooling, lead to an even grain size

wt %	C	Si	Mn	S	P	Fe
Tubes	0.71	0.2	0.5	0.003	0.03	98.4
Rails	0.76	0.2	0.9	0.02	0.02	98.0

Table 1: Mean chemical composition of heat-treated tubes in comparison to R260 rails.

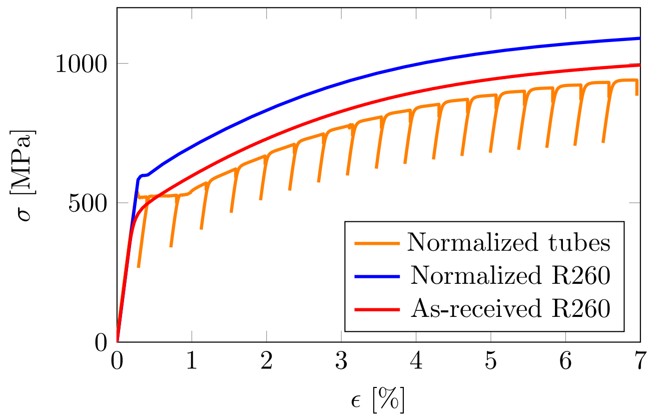

Figure 2: Stress strain behavior of railway steel R260 and heat treated cold-drawn tubes.

throughout the wall thickness (Figure 1c). The two heat treatments yielded a slight deviation in roundness, meaning that exact cross sections were difficult to measure. However, based on the well-documented Young's modulus of pearlitic steel of 210 GPa, the cross-sectional area could be easily obtained from the slope of the elastic range of the uniaxial loading curve.

2.2. Stress-strain behavior

Upon yielding, the normalized test tubes experience a drop in the flow stress, followed by a plateau phase, see Figure 2 (the regular unloading is nearly elastic and can be disregarded). While such behavior is well known for ferritic steels, cf. e.g. Lomer (1952), it is less common for pearlitic steels. Figure 2 shows that the pearlitic R260 steel (EN13674-1 (2011), as received) behaves very different upon yielding. The R260 samples were extracted from manufactured rails, see Meyer et al. (2018) for details. Rail straightening during the manufacturing induces some plastic deformations, which could explain the more gradual elastic-to-plastic transition. Normalizing the R260 sample causes stress plateauing, although it is less pronounced than for the normalized tubes. This observation is in accordance with the findings of Wang et al. (2020), who found that annealing pearlitic steels only results in stress plateauing after cold working. Table 1 shows that the rail material has more manganese and slightly higher carbon content. Manganese gives a solid solution strengthening of the ferrite phase, while more carbon results in a higher cementite fraction. Consequently, the normalized rail material has higher flow stress than the tube material. Furthermore, a higher cooling rate than during the rail production explains the increased flow stress after normalization of the rail material. Despite these differences in composition, cooling rate, and flow stresses, all test samples show similar hardening behavior after the initial plateau.

3. Material modeling

This section presents the material modeling framework and how to connect it to the experimental results. Since many different approaches for modeling finite strain plasticity exist in the literature, we consider only the small strain notation in this paper. The geometrical changes are accounted for by calculating the true stresses and strains from the experiments, see Appendix A. However, the analysis is also applicable to finite strain models, exemplified for a specific finite strain model in Appendix B.

3.1. General material modeling framework

The models assume a quadratic yield criterion of the form

$$\Phi = \sqrt{\boldsymbol{\sigma}_{\mathrm{red}} : \mathbf{C} : \boldsymbol{\sigma}_{\mathrm{red}}} - (Y_0 + \kappa) \leq 0 \tag{1}$$

where Y_0 is the initial yield limit, κ the isotropic hardening stress, and $\mathbf{C}$ a 4th order anisotropy tensor that may evolve during plastic deformation. $\boldsymbol{\sigma}_{\mathrm{red}}$ is the reduced stress, i.e.

$$\boldsymbol{\sigma}_{\mathrm{red}} = \boldsymbol{\sigma} - \boldsymbol{\beta} \tag{2}$$

where $\boldsymbol{\beta}$ is the back-stress due to kinematic hardening (Bauschinger effect) and $\boldsymbol{\sigma}$ the Cauchy stress. An additive decomposition of the strain, $\boldsymbol{\epsilon}$, into elastic, $\boldsymbol{\epsilon}_{\mathrm{e}}$, and plastic, $\boldsymbol{\epsilon}_{\mathrm{p}}$, parts is assumed, along with a linear elastic response, i.e.

$$\boldsymbol{\epsilon} = \boldsymbol{\epsilon}_{\mathrm{e}} + \boldsymbol{\epsilon}_{\mathrm{p}} \tag{3}$$

$$\boldsymbol{\sigma} = \mathbf{E} : \boldsymbol{\epsilon}_{\mathrm{e}} \tag{4}$$

where $\mathbf{E}$ is the 4th order elasticity tensor. Furthermore, we assume associative evolution of the plastic flow according to

$$\dot{\boldsymbol{\epsilon}}_{\mathrm{p}} = \dot{\lambda}\frac{\partial \Phi}{\partial \boldsymbol{\sigma}} \tag{5}$$

Here, the plastic multiplier, $\dot{\lambda}$, is the rate of the accumulated plasticity, given by the standard KKT-conditions for rate-independent plasticity, i.e.

$$\Phi \leq 0, \quad \dot{\lambda} \geq 0, \quad \Phi\dot{\lambda} = 0 \tag{6}$$

3.2. Isotropic hardening laws

The two most common isotropic hardening laws for cyclic metal plasticity are the Voce-law and the Swift power-law. These can be formulated as

$$\text{Voce:}\, \kappa = \kappa_\infty \left[1 - \exp\left(\frac{H_{\mathrm{iso}}}{\kappa_\infty}\lambda\right)\right] \tag{7}$$

$$\text{Swift:}\, \kappa = K\left[e_0 + \lambda\right]^n \tag{8}$$

Some authors also combine these two laws, and even further generalizations are possible, cf. Ristinmaa et al. (2007). However, the common denominator for all these models, is that they postulate that κ is a function of the accumulated plasticity λ,

$$\lambda = \int_0^t \dot{\lambda}\mathrm{d}t \tag{9}$$

In Chaboche (1986), such models are denoted "Classical isotropic hardening". The concept of "Maximum plastic strain memory" was introduced in Chaboche et al. (1979), introducing a so-called "non-hardening surface in the plastic strain space". This modification was motivated by the need to obtain different saturated peak stresses for different strain amplitudes. However, this correlates only approximately with isotropic hardening; see Equation 118 in Chaboche et al. (1979). Although the results show significant improvements, the suggested approach is rarely applied in modern literature. Some exceptions are El Abdi et al. (1999); Zhou et al. (2018). Some authors, e.g. Park et al. (2019), have adopted the alternative of using the plastic work in place of the accumulated plasticity, λ, suggested in Lemaitre and Chaboche (1990).

3.3. Distortional hardening laws

Many models for distortional hardening employ a yield surface described by Equation (1), e.g. Feigenbaum and Dafalias (2007); Barthel et al. (2008); Noman et al. (2010); Pietryga et al. (2012); Shi et al. (2014). Typically, the evolution of the $\mathbf{C}$ is governed by $\boldsymbol{n} \otimes \boldsymbol{n}$ and $\boldsymbol{\beta}$, where

$$\boldsymbol{n} = \frac{\boldsymbol{\sigma}_{\mathrm{red}}^{\mathrm{dev}}}{\left|\left|\boldsymbol{\sigma}_{\mathrm{red}}^{\mathrm{dev}}\right|\right|} \tag{10}$$

Terms involving only the back-stress $\boldsymbol{\beta}$ are typically responsible for the high curvature in the loading direction observed in many experiments, e.g. Naghdi et al. (1958); Phillips and Juh-Ling (1972). However, as shown by Khan and Wang (1993), this effect is only present when a small plastic strain offset is used to define the yield points. As discussed in Section 4, such low offsets are not relevant for most engineering applications and are not employed in the present study. Barthel et al. (2008); Noman et al. (2010) do not include the high curvature in the loading direction. In Pietryga et al. (2012); Shi et al. (2014) it can be removed by setting a parameter to zero (c_{H} and b_{C} respectively). The terms involving $\boldsymbol{n}$ are typically split into two parts, $\mathbf{N} = \boldsymbol{n} \otimes \boldsymbol{n}$ and $\mathbf{N}_\perp = \mathbf{I}^{\mathrm{dev}} - \mathbf{N}$, e.g.

$$\dot{\mathbf{C}} = \dot{\lambda}\left[h_{\|}(\mathbf{C}, \mathbf{N})\mathbf{N} + h_{\perp}(\mathbf{C}, \mathbf{N})\mathbf{N}_{\perp}\right] \tag{11}$$

$$\mathbf{C}(t=0) = \frac{3}{2}\mathbf{I}^{\mathrm{dev}}$$

where $\mathbf{I}^{\mathrm{dev}} = \mathbf{I} - \boldsymbol{I} \otimes \boldsymbol{I}/3$. $\mathbf{I}$ and $\boldsymbol{I}$ are the 4th and 2nd order identity tensors. While some works consider an initial anisotropy, the samples considered herein are initially isotropic, and the initial condition for $\mathbf{C}$ is chosen accordingly. The first term, along $\mathbf{N}$, is responsible for self-hardening, i.e. the hardening in the current loading direction. The second term, along $\mathbf{N}_\perp$, results in cross-hardening, i.e. hardening in directions perpendicular to the current loading direction. Self- and cross-hardening are also denoted by dynamic and latent hardening in the literature. If proportional loading along the fixed stress direction $\boldsymbol{n}_0$ is considered, i.e.

$$\boldsymbol{\sigma}(t) = f(t)\boldsymbol{n}_0 \tag{12}$$

the back-stress, $\boldsymbol{\beta}$, is co-linear with the deviatoric stress, $\boldsymbol{\sigma}^{\mathrm{dev}} = \mathbf{I}^{\mathrm{dev}} : \boldsymbol{\sigma}$, for all kinematic hardening laws known by the authors. Hence, the reduced stress may be expressed as

$$\boldsymbol{\sigma}_{\mathrm{red}}^{\mathrm{dev}}(t) = f_{\mathrm{red}}(t)\boldsymbol{n}_0^{\mathrm{dev}} \tag{13}$$

causing $\mathbf{N}$ and $\mathbf{N}_\perp$ to be constant. For such a case, the anisotropy tensor $\mathbf{C}$ depend only on the accumulated plasticity, λ. Thus, for proportional loading the distortional hardening in many models is also governed by λ.

3.4. Measuring the plastic multiplier

In the models considered herein, $\mathbf{C}$ is not a direct function of $\boldsymbol{\sigma}$, although its evolution may be. This implies that $\frac{\partial \mathbf{C}}{\partial \boldsymbol{\sigma}} = 0$, and the evolution of the plastic strains may be calculated as

$$\dot{\boldsymbol{\epsilon}}_{\mathrm{p}} = \dot{\lambda}\frac{\partial \Phi}{\partial \boldsymbol{\sigma}} = \dot{\lambda}\frac{\mathbf{C} : \boldsymbol{\sigma}_{\mathrm{red}}}{\sqrt{\boldsymbol{\sigma}_{\mathrm{red}} : \mathbf{C} : \boldsymbol{\sigma}_{\mathrm{red}}}} \tag{14}$$

Assuming that we only have proportional loading according to Equation (13) and by using Equation (11), $\mathbf{C}$ can be expressed as

$$\mathbf{C} = \frac{3}{2}\mathbf{I}^{\mathrm{dev}} + k_{\parallel}(\lambda)\mathbf{N} + k_{\perp}(\lambda)\mathbf{N}_{\perp} \tag{15}$$

where the functions $k_{\parallel}(\lambda)$ and $k_{\perp}(\lambda)$ also depend on the material parameters. Insertion into Equation (14) yields

$$\dot{\boldsymbol{\epsilon}}_{\mathrm{p}} = \dot{\lambda}\,\mathrm{sign}(f_{\mathrm{red}}(t))\sqrt{\frac{3}{2} + k_{\parallel}(\lambda)}\,\boldsymbol{n}_0^{\mathrm{dev}} \tag{16}$$

Meyer and Menzel (2021) obtained better results by replacing the self-hardening contribution with one additional isotropic hardening stress. As seen here, this choice affects the model behavior regarding the plasticity accumulation, λ. Letting $k_{\parallel}(\lambda) = 0$, following Meyer and Menzel (2021), enables a direct calculation of λ from the experimental results. For the analysis in the present paper, we assume $k_{\parallel}(\lambda) = 0$, but explain at the end of Section 5.1 how the general expression in Equation (16) when $k_{\parallel}(\lambda) \neq 0$ does not affect our conclusions.

Finally, note that for axial loading, $\boldsymbol{n}_0^{\mathrm{dev}} = [2/3, -1/3, -1/3, 0, 0, 0]$. Hence, the increment of plasticity is $\Delta\lambda = \sqrt{3/2}|[\Delta\epsilon_{\mathrm{p}}]_{11}|$ during a monotonic change of $[\epsilon_{\mathrm{p}}]_{11}$. Using the additive decomposition, Equation (3), and the linear elastic law, Equation (4), yields

$$[\epsilon_{\mathrm{p}}]_{11} = \epsilon_{11} - \frac{\sigma_{11}}{E} \tag{17}$$

where E is the axial stiffness modulus (Young's modulus in the case of isotropy). For improved accuracy, the stiffness E is calibrated for the start of the specific load segment (up to a stress change of 100 MPa). The plastic strain increment is then calculated as

$$[\Delta\epsilon_{\mathrm{p}}]_{11} = [\epsilon_{\mathrm{p}}]_{11}(t_{i+1}) - [\epsilon_{\mathrm{p}}]_{11}(t_i) \tag{18}$$

Here, t_i and t_{i+1} are the times at the start and end of the load segment, respectively.

4. Experimental setup

We use an axial-torsion testing machine with transducer capacities 100 kN and 1100 Nm. The biaxial extensometer can measure an axial strain $\epsilon \in [-0.04, 0.10]$ and a surface shear strain $\gamma = \pm 0.04$. The tubular test bars with outer diameter 20 mm and thickness 1.5 mm are described in Section 4.1. While the results are compensated for large strains according to Appendix A, the loading parameters are set in terms of the engineering stresses and strains.

Each experiment consists of a probing sequence followed by a loading sequence. The probing sequence measures the axial and shear yield strengths, and is described below in Section 4.2. As discussed in Section 3, the identification procedure relies on proportional loading. Therefore, we ensure that the plastic shear strains are small during the probing sequence. The individual experiments are characterized by their specific loading sequence. It can be either cyclic loading with different strain amplitudes or monotonic loading. The specific parameters are described in Section 4.3.

4.1. Test bar geometry

As previously discussed in Section 2, we use heat-treated, cold-drawn tubes as test bars. Figure 3 shows how the tubes are mounted in the testing machine. The outer sleeve is made from hardened steel and is slotted on the rear side to improve the grip. To avoid stress concentrations at the end of the sleeve, it is not slotted next to the gauge section and extends outside the machine grips. The green plug in the center prevents excessive deformations due to the gripping force.

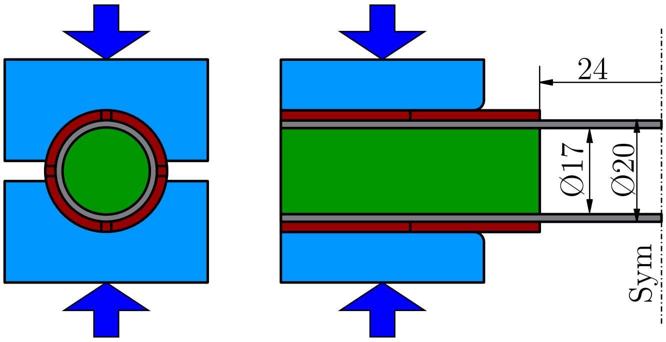

Figure 3: Tube specimen (gray) with inner plugs (green), outer sleeves (red), and machine grips (light blue). The grip force exerted by the machine is shown by blue arrows. All dimensions in mm.

4.2. Yield probing sequence

Most papers on yield surface measurements use deviation from linearity to detect yielding, see e.g. Naghdi et al. (1958); Phillips et al. (1972); Moreton et al. (1978). While these studies had the operator deciding when to stop, more modern studies include automated yield detection, cf. Sung et al. (2011). However, these studies also rely on an offset from linearity. One potential drawback of this criterion is the assumption of linear elastic deformations. As shown by Sommer et al. (1991), this assumption may lead to incorrect results for high-strength steels. Additionally, the regression of the stress-strain response in an assumed linear region introduces additional uncertainties. We avoid these issues by measuring the residual plastic strains via loading and unloading during probing. However, upon unloading after cyclic loading the material can plasticize slightly. To prevent this phenomenon, we increment the stress unloading level.

Figure 4 shows the beginning of a probing sequence in the compressive axial direction. During the last 3 s of the 4 s time intervals m_{ij}, the average strains are measured. The first index, i, represents the current reference (unloading) level. The second index, j, counts the measurement number at the current reference level. Letting the material relax for 1 s, and then taking the average strains during 3 s, decreases the measurement scatter. m_{ij}^{ϵ} and m_{ij}^{γ} denote these averaged axial and shear strains. The peak axial and shear stresses prior to m_{ij} are recorded at p_{ij} and denoted p_{ij}^{σ} and p_{ij}^{τ}, respectively. The first measurement interval, m_{00}, is used as a reference point where the plastic strain increment is zero by definition. After N steps, corresponding to a 25 MPa increase in probing stress, the reference level is changed. Hence, the plastic strain $\epsilon_{\mathrm{p}}^{ij}$ at m_{ij} can be calculated as

$$\epsilon_{\mathrm{p}}^{ij} = m_{ij}^{\epsilon} - m_{i0}^{\epsilon} + \sum_{k=0}^{i-1} \left[m_{kN}^{\epsilon} - m_{k0}^{\epsilon} \right] \tag{19}$$

Each term in the sum in Equation (19) adds to the uncertainty of the strain measurements. Therefore, we did not choose a lower reference step than 25 MPa. In other loading directions, the von Mises effective stress is used. The plastic shear strain, γ_{p}^{ij} is calculated equivalently to Equation (19).

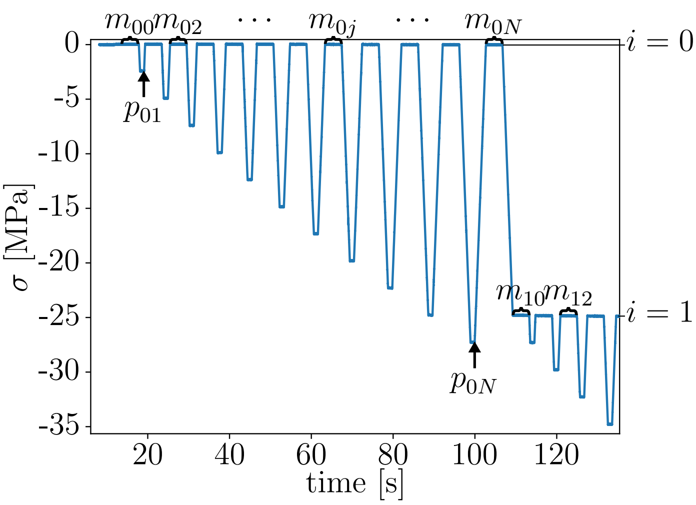

Figure 4: Probing sequence.

Many measured yield surfaces exclude the origin due to a translation along the axial stress direction. In such cases, we observed some ratcheting in the axial direction when measuring the shear yield limit. To prevent these strains from influencing the offset strain definition, the plastic strain is projected onto the stress direction (which was controlled). The stress during probing may be described as

$$\sigma = \sigma_{\mathrm{vM}}(t)\cos(\alpha) + \sigma_0 \tag{20}$$
$$\tau = \sigma_{\mathrm{vM}}(t)\sin(\alpha)/\sqrt{3} + \tau_0 \tag{21}$$

for a probe direction α and with a load origin (σ_0, τ_0). Then, the effective plastic offset strain is calculated as

$$\epsilon_{\mathrm{p}}^{\mathrm{offset},ij} = \epsilon_{\mathrm{p}}^{ij}\cos(\alpha) + \gamma_{\mathrm{p}}^{ij}\sin(\alpha)/\sqrt{3} \tag{22}$$

Choosing the limit value of the offset strain $\epsilon_{\mathrm{p}}^{\mathrm{offset}}$ is governed by contradictory requirements. A lower value reduces the influence on subsequent measurements and by causing lower plastic shear strains. The latter is vital for testing the validity of the accumulated plasticity's effect on the shear yield strength. When studying microstructural yielding processes, the onset of yielding may be of primary interest. Figure 5 shows yield points calculated by different offset definitions. In the first cycle, the 0.001 % offset yield point occurs at a much lower stress than when the bulk material plasticizes. When considering the cyclic plastic behavior during, e.g., low cycle fatigue analyses, the plasticizing of the bulk material has more influence than the onset of yielding. In the second cycle, the material has undergone some plastic deformation. This history causes a smoother elastic to plastic transition without a distinct yield point. However, in the author's experience, calibrated models in the literature typically do not capture the non-linearity prior to the 0.01 % offset point. Hence, we consider this point a reasonable compromise for the present study.

The first probe is along $\alpha = -\pi$ to measure σ_{p1}, with $\tau_0 = 0$ and $\sigma_0 = \sigma_{p0}$. Here, σ_{p0} is the current stress at the end of the previous loading cycle. The center of the yield surface is then given by $\tau_0 = 0$ and $\sigma_0 = [\sigma_{p0} + \sigma_{p1}]/2$, and then we probe in directions $\alpha = \pm\pi/2$ to find the shear yield strength.

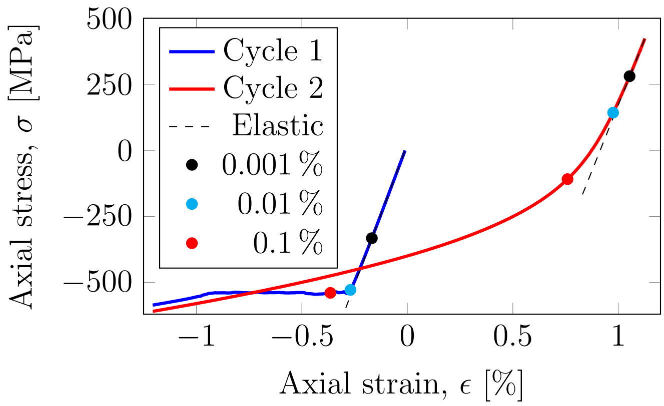

Figure 5: Stress-strain curve with different offset strain yield points.

4.3. Proportional loading sequences

To test the modeling hypotheses identified in Section 3 during cyclic loading, we require a range of strain amplitudes. The results in Figure 5 show the material's distinct yield at about 528 MPa, corresponding to a strain of 0.27 %. However, some plasticity occurs before this point. Due to the significant cyclic softening of the material, a hysteresis loop developed after the first cycle at $\epsilon = \pm 0.25\,\%$, see Figure 9a. In addition to $\pm 0.25\,\%$, we chose strains $\pm 0.40\,\%$, $\pm 0.80\,\%$, and $\pm 1.20\,\%$. Furthermore, the modeling hypothesis can also be tested for monotonic loading. During this loading, yield surface measurements occur each 0.4 % strain increment (see Figure 8).

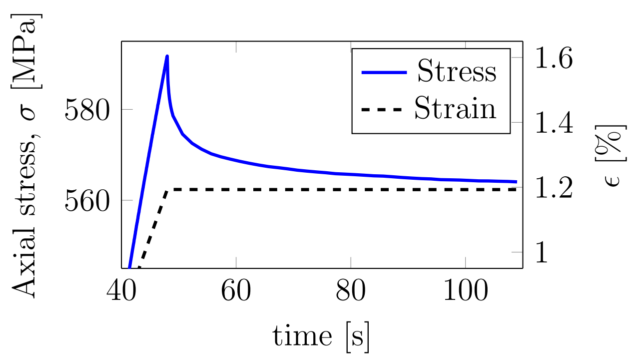

Figure 6: Stress versus time during the hold time after the first loading cycle.

Even at room temperature, the material exhibits some relaxation after cyclic loading, as shown by Figure 6. Therefore, a hold time of 1 min follows each loading before starting the

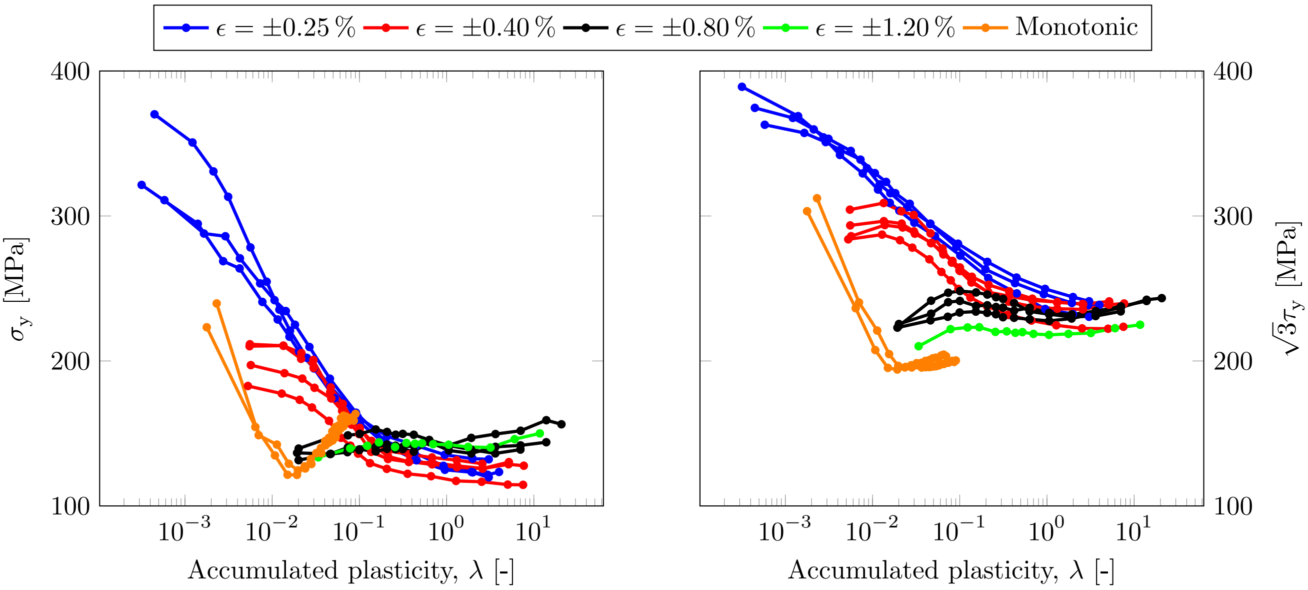

(a) Axial yield stress.

(b) Shear yield stress.

Figure 7: Yield surface evolution as a function of the accumulated plasticity for monotonic and different cyclic load amplitudes.

yield surface measurements. The cyclic loading rate was 0.025 %/s, and the stress loading rate was 10 MPa/s during the probing.

5. Results and discussion

The main objective of the present paper is to investigate yield surface evolution during proportional cyclic and monotonic loading. Hence, these results are presented first. To further understand the results and the material behavior, the cyclic stress-strain responses are discussed thereafter. Finally, we discuss how our findings should influence future cyclic plasticity models.

5.1. Yield evolution

Figures 7a and 7b show how the yield stress evolves with the accumulated plastic deformation λ. According to the standard modeling hypothesis, the isotropic yield stress should evolve equally for all loading types. Without distortional hardening, the axial yield stress in Figure 7a shows the isotropic yield stress evolution. And as discussed in Section 3, quite some distortional hardening models predict the same. Such models also assume that the cross-hardening response, here shown by the shear yield stress evolution, should only depend on λ for proportional loading.

Figure 7a shows that λ alone cannot describe the axial yield stress evolution. For cyclic loading and an accumulated plasticity $\lambda < 0.1$, the axial yield stress evolution depends strongly on the strain amplitude. While the differences are large for amplitudes between 0.25 % and 0.8 %, no significant difference is observed between 0.8 % and 1.2 %. At higher λ values, the differences between the strain amplitudes are much smaller. Still, there is a tendency that the high strain amplitudes (0.8 and 1.2 %) show a cyclic hardening for $\lambda > 1$. The lower amplitudes (0.25 and 0.4 %) show a continued cyclic softening, although many orders of magnitudes less than the initial softening (note the logarithmic λ-axis).

The shear yield stress evolution in Figure 7b shows a similar trend to the axial yield stress. Scaling the τ-axis by $\sqrt{3}$ results in the equivalent von Mises stress, enabling comparisons to the axial yield stress. After the first cycle of 0.25 % strain amplitude, the von Mises yield stresses are similar in the axial and shear directions. As for the axial results, the shear yield stresses are similar after many cycles for different strain amplitudes. However, the von Mises yield stress is much higher than the corresponding axial yield stress, indicating an anisotropic yield surface. A notable difference to the axial response, is that the 1.2 % strain amplitude results in a lower yield stress than the 0.8 % amplitude.

The monotonic responses in Figure 7 are different from the cyclic responses: The initial yield limit is about 500 MPa. Until $\lambda = 0.01$, the yield stress decreases for all loading cases. However, after this, the monotonic response show an increasing yield stress. The high amplitude load cases have a fairly constant yield stress, while the low amplitude cases keep reducing the yield limit. For shear stresses, the behavior is similar, but less pronounced. The extensometer's strain range limits the maximum accumulated plasticity during monotonic loading.

The accumulated plasticity, λ, in Figure 7, was calculated by assuming $k_{\|}(\lambda) = 0$ in Equation (16). Without this assumption, it is impossible to calculate λ from the experiments as it depends on material parameters. However, as $k_{\|}(\lambda)$ only depends on λ and material parameters for proportional loading, $k_{\|}(\lambda) \neq 0$ would only result in a non-uniform scaling of the x-axis. Therefore, the differences between the yield stresses would not change for such models.

5.2. Monotonic response

As discussed in Section 2, the material exhibits a stress plateau after an initial peak during monotonic loading. Figure 8 shows the two tests for monotonic loading. The second test, shown with a dotted line, was restarted due to a computer failure during the first axial probing sequence. The restart resulted in slightly more accumulated compressive plastic strains before the first cycle. These strains explain why the behavior during the first cycle differs from the first test (solid line). After this first cycle, both tests show similar results on the overall stress-strain response.

The solid markers with the axial yield limits, σ_y, show the initial isotropic softening followed by hardening. The start point of each step shows the current yield center, i.e. β, governed by the kinematic hardening. The stress curve is the sum of these two contributions. Hence, the initial plateau

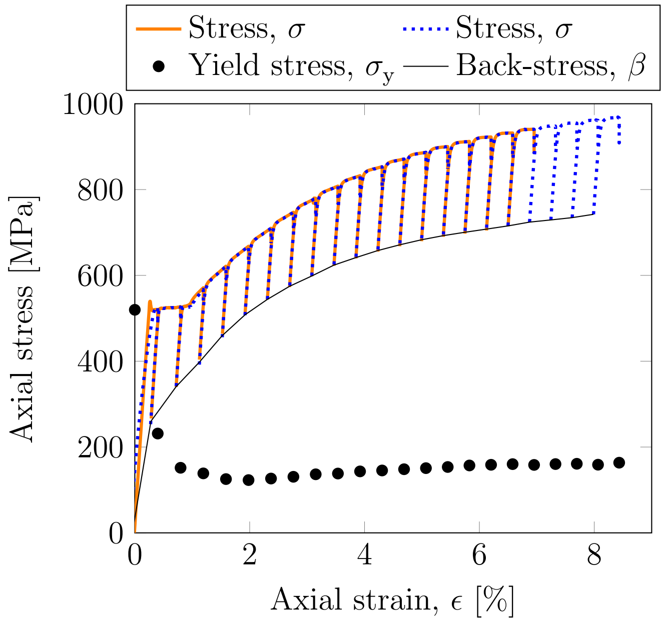

Figure 8: Two monotonic experiments, where each new step starts from the identified yield surface center, $\sigma = \beta$.

seem to occur due to the competing effects of a rapid isotropic softening and kinematic hardening. The kinematic hardening continues to harden with decreasing rate. When isotropic softening decreases, the peak stress begin increasing. While isotropic hardening can explain a small part of the stress increase, most is due to the continued kinematic hardening.

5.3. Hysteresis loops

The first hysteresis loop in Figure 9a is almost fully elastic. At the end of the cycle, it seems to pass over the initial peak observed in e.g. Figure 8. In the second cycle, the wider loop shape shows more plasticity. The lack of any stress plateau is very different from the monotonic stress-strain response, even though the amount of plasticity is similar. Hence, it seems that the load reversal strongly impacts the material response. The behavior with an initial peak followed by a rapid softening makes the experiments sensitive to any heterogeneities in the test bars. If some parts yield before others, the global stress-strain response might not exhibit such a peak. Therefore, results at small plastic deformations before this peak must be analyzed with care, as this sensitivity introduces additional uncertainty in the

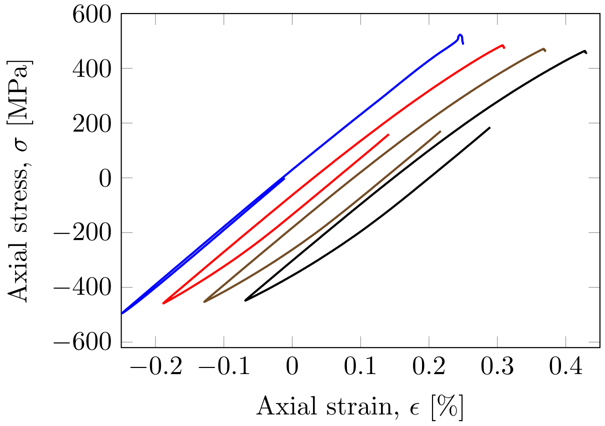

(a) First 4 cycles for $\epsilon = \pm 0.25\,\%$. Each cycle is shifted $0.06\,\%$ from the previous for better visibility (1 test bar).

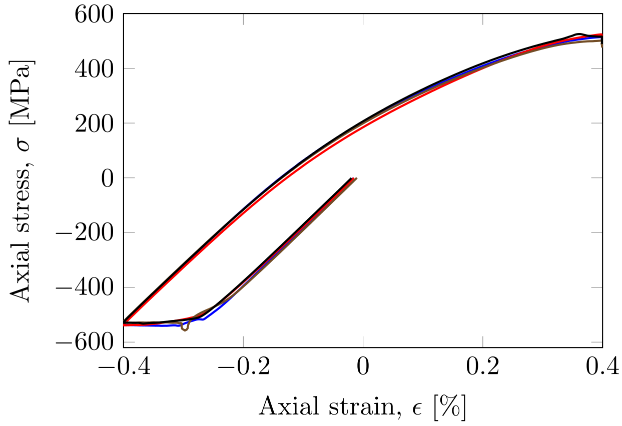

(b) First cycle for $\epsilon = \pm 0.40\,\%$ (4 test bars).

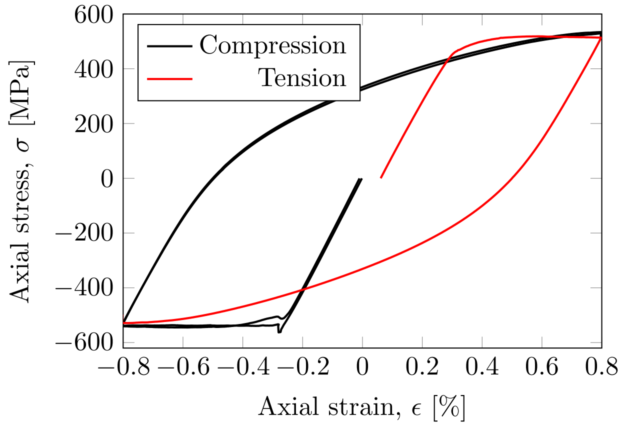

(c) First cycle for $\epsilon = \pm 0.80\,\%$ (3 test bars).

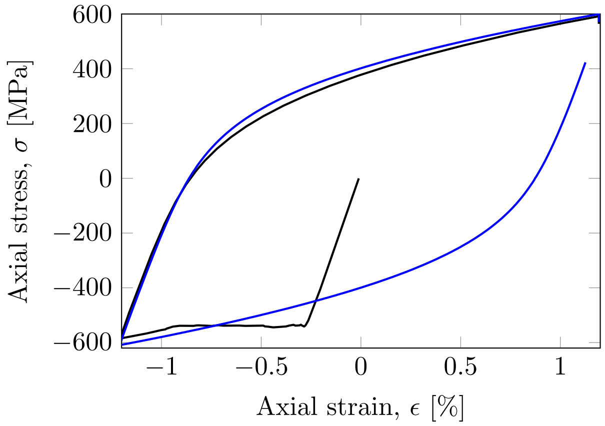

(d) First 2 cycles for $\epsilon = \pm 1.20\,\%$ (1 test bar).

Figure 9: Initial hysteresis loops for different strain amplitudes.

experimental results. However, after some plastic deformations, the material responses show less spread. This observation is illustrated clearly by Figure 7a, where the measurement uncertainty decrease with more plastic deformations.

For 0.4 and $0.8\,\%$ strain amplitude, Figures 9b and 9c, there are significant plastic strains already in the first cycle. Some experiments show similar behavior to the monotonic experiment in Figure 8 exhibiting an initial peak. However, the uncertainties during this initial loading phase are highlighted by Figures 9b and 9c. While all experiments show the plateau phase, not all show a clear initial peak. In some experiments, the machine grips were not perfectly aligned, causing small bending stresses in the samples. These stresses affect the initial plasticity, but the results after the first cycle do not seem to have been affected. The tensile-first experiment in Figure 9c was conducted before alignment, while the monotonic experiments in Figure 8 were conducted after alignment. Overall, at least one experiment after alignment was performed for each test condition. No clear effect was observed on the yield evolution. Therefore, we also include the results from experiments conducted before the alignment.

The stress during the first cycle for the $1.2\,\%$ strain amplitude plateaus after yielding until about $-0.9\,\%$ strain, and then hardening occurs. This response is similar to that in Figure 8. After this initial phase, a smooth elastic-to-plastic transition occurs in each cycle.

5.4. *Peak stress evolution*

For the monotonic stress-strain response in Figure 8, we previously concluded that the Bauschinger effect caused most of the hardening.

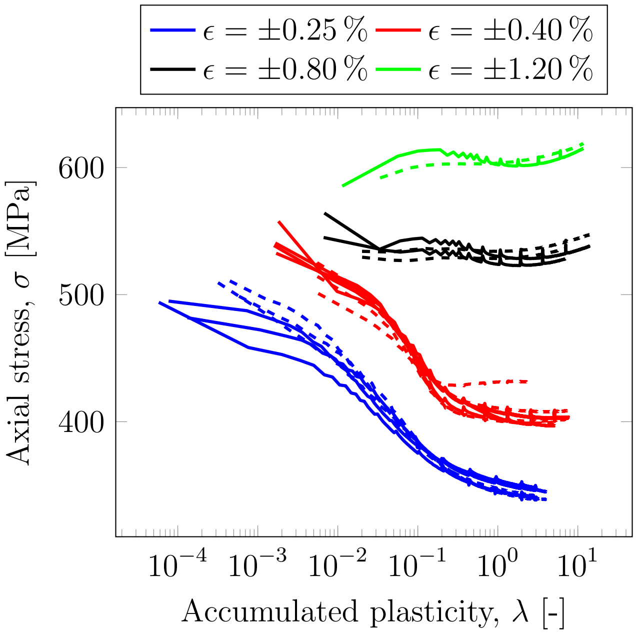

Figure 10: Peak (dashed) and valley (absolute value, solid) axial stress evolution.

The peak and valley stress evolutions in Figure 10 support this conclusion as no large increase in stress ranges occurs. Based on the axial yield stress evolution, we could observe a slight hardening tendency for the high amplitudes. The results in Figure 10 reinforces this finding. Furthermore, these results also show the previously observed continued softening for low strain amplitudes. A similar behavior is also observed in Fig. 4 in Ahlström and Karlsson (2005) for the pearlitic rail grade 900A.

5.5. Discussion of implication for future models

The results show that the common assumption that the yield surface size depends only on the accumulated plasticity leads to incorrect model predictions. Of course, there may exist materials for which this assumption holds, as our results only consider one pearlitic steel. Previously, we mentioned the rarely used concept of "Maximum plastic strain memory" introduced by Chaboche et al. (1979). This extension should account for the different stabilized isotropic hardening for different plastic strain amplitudes. However, our results show similar stabilized isotropic hardening for different amplitudes. Instead, the evolution before an approximate stable cycle depends on the strain amplitude. Hence, the "Maximum plastic strain memory" strategy does not capture this material behavior. One important observation from our results is the qualitative similarity between the axial and shear yield stress evolution. This finding indicates that similar evolution laws may be used, although with different parameters.

As mentioned in Section 5.2, the plateau effect can be seen as a competing effect of isotropic softening and kinematic hardening. Such a response can be approximated by a standard material model with rapid isotropic softening balanced by an approximately equally strong kinematic hardening with higher saturation stress. However, as previously stated, isotropic hardening cannot be specified as a function of only the accumulated plasticity, λ, when modeling different load cases. Adding multiple isotropic hardening stresses as in Qin et al. (2018); Meyer and Menzel (2021) cannot solve this problem. Other state variables are required in the evolution laws for isotropic and distortional hardening.

6. Contributions

The yield surface evolution during cyclic and monotonic loading has been studied. In particular, we question how many cyclic plasticity models assume that the isotropic yield strength only depends on the accumulated plasticity. Our results reveal that this assumption does not hold for the investigated steel. Furthermore, we show that many distortional hardening models predict the same behavior for cross-hardening during proportional loading. However, according to our results, the accumulated plasticity cannot capture cross-hardening for different loading cases. Adding multiple hardening stresses cannot solve the identified discrepancies. Instead, our findings clarify the need for new evolution laws to obtain more accurate models.

7. Acknowledgements

The major part of this work was conducted within the CHARMEC Centre of Excellence at Chalmers University of Technology. Parts of the study have been funded within the Shift2Rail Joint Undertaking in European Union's Horizon 2020 research and innovation programme in the project In2Track2 and In2Track3 under grant agreements nos. 826255 and 10102456. K. A. Meyer has moved from Chalmers University of Technology to TU Braunschweig during the finalization of this paper.

8. CRediT

K.A.Meyer: Conceptualization, Methodology, Formal analysis, Investigation, Writing - Original Draft, Visualization **J.Ahlström:** Investigation, Writing - Original Draft

A. True stress and strain calculation

In order to estimate the true stresses, σ and τ, linear elasticity wrt. to the logarithmic axial strain, ϵ, using constant parameters, $E = 210\,\mathrm{GPa}$ and $\nu = 0.3$, is assumed. We measure the stresses $P_\sigma = F/A$ and $P_\tau = T/(AR)$ based on the force, F, torque T, initial area A, and initial mean radius R. The engineering strains $\tilde{\epsilon} = \Delta L/L$ and $\gamma = r\Delta\phi/L$ are also measured.

$$\epsilon = \ln(1 + \tilde{\epsilon}) \tag{23}$$

$$\epsilon_\mathrm{e} \approx P_\sigma/E, \quad \epsilon = \epsilon_\mathrm{e} + \epsilon_\mathrm{p} \tag{24}$$

$$\epsilon_{rr} = \epsilon_{\theta\theta} = -\nu\epsilon_\mathrm{e} - 0.5\epsilon_\mathrm{p} \tag{25}$$

The elastic strain ϵ_e is small. Hence, the error introduced by the approximation in Equation (24) on the transverse strains in Equation (25) is acceptable. Note that the compensated stress is used when calculating the plastic strains in Equation (17) for measuring the accumulated plasticity. Equation (25) uses the plastic incompressibility following the associative plastic evolution law in Equation (5)

The updated area a can then be calculated from the undeformed area A as

$$a = A\left[1 - \nu\epsilon_\mathrm{e} - 0.5\epsilon_\mathrm{p}\right]^2 \tag{26}$$

and the updated mean radius r from the original radius R as

$$r = R\left[1 - \nu\epsilon_\mathrm{e} - 0.5\epsilon_\mathrm{p}\right] \tag{27}$$

This gives the updated stresses

$$\sigma = \frac{P_\sigma}{\left[1 + [0.5 - \nu]\,\frac{P_\sigma}{E} - 0.5\epsilon\right]^2} \tag{28}$$

$$\tau = \frac{P_\tau}{\left[1 + [0.5 - \nu]\,\frac{P_\sigma}{E} - 0.5\epsilon\right]^3} \tag{29}$$

B. Finite strain formulation

In this paper we presented method for identifying the accumulated plastic deformation directly from experimental data. However, the analysis was based on a linear kinematics, or a small strain analysis. For large plastic deformations, a finite strain model may be required. In this appendix, we show that the same approach can be used in the case of a finite strain model, although the derivations are more involved. To this end, we use the model proposed in Meyer and Menzel (2021) as an example.

B.1. Model description

First, we briefly describe the model denoted $H_\mathrm{r} = 0$ in Meyer and Menzel (2021). It has a multiplicative split of the deformation gradient; $\boldsymbol{F} = \boldsymbol{F}_\mathrm{e}\boldsymbol{F}_\mathrm{p}$. Based on a Neo-Hookean formulation, the Mandel stress $\boldsymbol{M}$ is

$$\boldsymbol{M} = \frac{G\boldsymbol{C}_\mathrm{e}^\mathrm{dev}}{\mathrm{I}_{3C_\mathrm{e}}^{1/3}} + K\left[\mathrm{I}_{3C_\mathrm{e}} - \sqrt{\mathrm{I}_{3C_\mathrm{e}}}\right]\boldsymbol{I} \tag{30}$$

where $\boldsymbol{C}_\mathrm{e} = \boldsymbol{F}_\mathrm{e}^\mathrm{t}\boldsymbol{F}_\mathrm{e}$ and $\mathrm{I}_{3C_\mathrm{e}} = \det(\boldsymbol{C}_\mathrm{e})$. The yield criterion, $\Phi = 0$, is based on linear transformations to introduce anisotropy,

$$\begin{aligned} \Phi &= \sqrt{\frac{3}{2}\left[\boldsymbol{\mathsf{C}} : \boldsymbol{M}_\mathrm{red}\right]^\mathrm{t} : \left[\boldsymbol{\mathsf{C}} : \boldsymbol{M}_\mathrm{red}\right]} - [Y_0 + \kappa] \\ &= \sqrt{\boldsymbol{M}_\mathrm{red} : \hat{\boldsymbol{\mathsf{C}}} : \boldsymbol{M}_\mathrm{red}} - [Y_0 + \kappa] \\ \hat{\boldsymbol{\mathsf{C}}} &= \frac{3}{2}\boldsymbol{\mathsf{C}}^\mathrm{T} : [\boldsymbol{I}\underline{\otimes}\boldsymbol{I}] : \boldsymbol{\mathsf{C}} \end{aligned} \tag{31}$$

$\boldsymbol{M}_{\text{red}}$ is the Mandel stress reduced by the backstresses $\boldsymbol{M}_{\text{kin},i}$, i.e.

$$\boldsymbol{M}_{\text{red}} = \boldsymbol{M} - \sum_{i=1}^{N_{\text{back}}} \boldsymbol{M}_{\text{kin},i} \tag{32}$$

$$\boldsymbol{M}_{\text{kin},i} = \frac{H_{\text{kin},i}\boldsymbol{c}_{\text{kin},i}^{\text{dev}}}{\det\left(\boldsymbol{c}_{\text{kin},i}\right)^{1/3}} \tag{33}$$

where $\boldsymbol{c}_{\text{kin},i} = \boldsymbol{F}_{\text{kin},i}^{-\text{t}}\boldsymbol{F}_{\text{kin},i}^{-1}$. This introduces the kinematic deformation gradients $\boldsymbol{F}_{\text{kin},i}$. The non-standard open product $\underline{\otimes}$ is defined by $[\boldsymbol{a}\underline{\otimes}\boldsymbol{b}] : \boldsymbol{c} = \boldsymbol{a}\boldsymbol{c}^{\text{t}}\boldsymbol{b}^{\text{t}}$ where $\boldsymbol{a}$, $\boldsymbol{b}$, and $\boldsymbol{c}$ are 2nd order tensors.

The associative flow rule,

$$\dot{\boldsymbol{F}}_{\text{p}}\boldsymbol{F}_{\text{p}}^{-1} =: \boldsymbol{L}_{\text{p}} = \dot{\lambda}\boldsymbol{\nu}, \quad \boldsymbol{\nu} = \frac{\partial \Phi}{\partial \boldsymbol{M}} \tag{34}$$

and the non-associative kinematic hardening via $\boldsymbol{L}_{\text{kin},i} := \dot{\boldsymbol{F}}_{\text{kin},i}\boldsymbol{F}_{\text{kin},i}^{-1}$:

$$\boldsymbol{L}_{\text{kin},i} = \dot{\lambda}\left[-\boldsymbol{\nu} + \boldsymbol{\nu}_{\text{kin},i}^{*}\right]$$
$$\boldsymbol{\nu}_{\text{kin},i}^{*} = \delta\left[\sqrt{\boldsymbol{\nu}^{\text{t}} : \boldsymbol{\nu}}\right]\frac{\boldsymbol{M}_{\text{kin},i}^{\text{t}}}{B_{\infty,i}} + [1-\delta]\left[\frac{\boldsymbol{M}_{\text{kin},i} : \hat{\boldsymbol{\nu}}}{B_{\infty,i}}\right]\boldsymbol{\nu} \tag{35}$$
$$\hat{\boldsymbol{\nu}} = \frac{\boldsymbol{\nu}}{\sqrt{\boldsymbol{\nu}^{\text{t}} : \boldsymbol{\nu}}}$$

govern the evolution of $\boldsymbol{F}_{\text{p}}$ and $\boldsymbol{F}_{\text{kin},i}$. Isotropic hardening, $\kappa = \kappa_1 + \kappa_2$, has the form of Equation (8) for κ_1 and κ_2.

Similar to in Equation (14), $\boldsymbol{\nu}$ becomes

$$\boldsymbol{\nu} = \frac{\hat{\mathbf{C}} : \boldsymbol{M}_{\text{red}} + \boldsymbol{M}_{\text{red}} : \hat{\mathbf{C}}}{2\sqrt{\boldsymbol{M}_{\text{red}} : \hat{\mathbf{C}} : \boldsymbol{M}_{\text{red}}}} \tag{36}$$

The evolution of $\mathbf{C}$ governs the anisotropy, and does not include self-hardening, i.e.

$$\mathbf{C} = [1 - b_\perp]\,\mathbf{I}^{\text{dev}} + b_\perp \mathbf{C}_\perp \tag{37}$$
$$\dot{\mathbf{C}}_\perp = -\dot{\lambda}c_\perp\left[\mathbf{N}_\perp^{\text{T}} :: \mathbf{C}_\perp\right]\mathbf{N}_\perp \tag{38}$$
$$\mathbf{N}_\perp = \mathbf{I}^{\text{dev}} - \frac{\boldsymbol{M}_{\text{red}}^{\text{dev}} \otimes \left[\boldsymbol{M}_{\text{red}}^{\text{dev}}\right]^{\text{t}}}{\boldsymbol{M}_{\text{red}}^{\text{dev}} : \left[\boldsymbol{M}_{\text{red}}^{\text{dev}}\right]^{\text{t}}}$$

B.2. Identification of the accumulated plasticity

To identify the accumulated plasticity directly from experiments, we must be able to obtain $\dot{\lambda}$ using Equation (34). Hence, we must be able to calculate $\boldsymbol{F}_{\text{p}}$ and $\boldsymbol{\nu}$ in the experiment. In finite strains, it is important that the proportional loading occurs in a normal loading direction to avoid any rotations. We will therefore consider a uniaxial experiment. The Kirchhoff stress $\boldsymbol{\tau}$ and deformation gradient $\boldsymbol{F}$ are then

$$\boldsymbol{\tau} = \begin{bmatrix} 0 & 0 & 0 \\ 0 & 0 & 0 \\ 0 & 0 & s \end{bmatrix}, \quad \boldsymbol{F} = \begin{bmatrix} y & 0 & 0 \\ 0 & y & 0 \\ 0 & 0 & x \end{bmatrix} \tag{39}$$

where x is measured in the experiment, and y and s are not directly measured. We can measure a nominal axial stress, S, which is related to the Kirchhoff axial stress, $s = Sx$. Henceforth, we will denote a tensor of the form of $\boldsymbol{F}$; diagonal with equal 11 and 22 components, a 2-1-diagonal tensor. Such a tensor has two properties that we will use: Consider that $\boldsymbol{a}$ and $\boldsymbol{b}$ are 2-1 diagonal. Then, $\boldsymbol{ab}$ is also 2-1 diagonal, and there exists a scalar k such that $\boldsymbol{a}^{\text{dev}} = k\boldsymbol{b}^{\text{dev}}$.

In the elastic state, since $\boldsymbol{F}_{\text{e}} = \boldsymbol{F}$,

$$\boldsymbol{M} = \boldsymbol{F}_{\text{e}}^{\text{t}}\boldsymbol{\tau}\boldsymbol{F}_{\text{e}}^{-\text{t}} = \boldsymbol{F}^{\text{t}}\boldsymbol{\tau}\boldsymbol{F}^{-\text{t}}\boldsymbol{\tau} \tag{40}$$

follows from Equation (39)

Next, we perform one explicit integration step into the plastic regime from the onset of yielding. In this case, $\boldsymbol{M} = \boldsymbol{\tau}$, $\mathbf{C}_\perp = \mathbf{I}^{\text{dev}}$, and $\boldsymbol{M}_{\text{kin},i} = \mathbf{0}$, yielding

$$\boldsymbol{\nu} = \text{sign}(s)\begin{bmatrix} -0.5 & 0 & 0 \\ 0 & -0.5 & 0 \\ 0 & 0 & 1 \end{bmatrix} \tag{41}$$

Using this $\boldsymbol{\nu}$, we obtain the new $\boldsymbol{F}_{\text{p}}$ from Equation (34) as

$$\boldsymbol{F}_{\text{p}} = {}^{\text{old}}\boldsymbol{F}_{\text{p}} + \Delta\lambda\boldsymbol{\nu}\,{}^{\text{old}}\boldsymbol{F}_{\text{p}} \tag{42}$$

$\boldsymbol{F}_{\text{p}}$ is thus a 2-1-diagonal tensor if ${}^{\text{old}}\boldsymbol{F}_{\text{p}}$ is a 2-1-diagonal tensor. By induction (initial value $\boldsymbol{I}$), $\boldsymbol{F}_{\text{p}}$ will then remain 2-1-diagonal assuming $\boldsymbol{\nu}$ retains this property. Hence, we conclude that

$$\boldsymbol{F}_{\text{e}} = \begin{bmatrix} y_e & 0 & 0 \\ 0 & y_e & 0 \\ 0 & 0 & x_e \end{bmatrix} \tag{43}$$

resulting in $\boldsymbol{\tau} = \boldsymbol{M}$ during proportional uniaxial loading. To investigate whether $\boldsymbol{\nu}$ remains a 2-1-diagonal tensor, we must also consider the evolution of $\boldsymbol{M}_{\mathrm{kin},i}$ and $\hat{\mathsf{C}}$. Following Equation (35), we have

$$\boldsymbol{F}_{\mathrm{kin},i} = {}^{\mathrm{old}}\boldsymbol{F}_{\mathrm{kin},i} - \Delta\lambda \left[\boldsymbol{\nu} - \boldsymbol{\nu}^{*}\right] {}^{\mathrm{old}}\boldsymbol{F}_{\mathrm{kin},i} \tag{44}$$

and we obtain that $\boldsymbol{F}_{\mathrm{kin},i}$ retains its 2-1-diagonal property if $\boldsymbol{\nu}$ and $\boldsymbol{M}_{\mathrm{kin},i}$ also does. Subsequently $\boldsymbol{c}_{\mathrm{kin},i}$ is 2-1-diagonal and thus also $\boldsymbol{M}_{\mathrm{kin},i}$ (Equation (33)). The back-stress can then be expressed as $\boldsymbol{M}_{\mathrm{kin},i} = b\boldsymbol{M}^{\mathrm{dev}}$ where b is some scalar value. The evolution of $\mathsf{C}_{\perp}$ becomes $\mathsf{C}_{\perp} = \mathsf{I}^{\mathrm{dev}} + a\mathsf{N}_{\perp}$, yielding

$$\hat{\mathsf{C}} = \frac{3}{2}\left[\mathsf{I}^{\mathrm{dev}} + a\mathsf{N}_{\perp}^{\mathrm{T}}\right] : \left[\boldsymbol{I}\,\underline{\otimes}\,\boldsymbol{I}\right] : \left[\mathsf{I}^{\mathrm{dev}} + a\mathsf{N}_{\perp}\right] \tag{45}$$

With these updated tensors, we can now evaluate $\boldsymbol{\nu}$ to investigate its form. To that end, we first evaluate

$$\hat{\mathsf{C}} : \boldsymbol{M}_{\mathrm{red}} = \hat{\mathsf{C}} : \boldsymbol{M}_{\mathrm{red}}^{\mathrm{dev}} = \frac{3}{2}\left[\boldsymbol{M}_{\mathrm{red}}^{\mathrm{dev}}\right]^{\mathrm{t}} \tag{46}$$

and hence

$$\boldsymbol{\nu} = \mathrm{sign}(s[1-b]) \begin{bmatrix} -0.5 & 0 & 0 \\ 0 & -0.5 & 0 \\ 0 & 0 & 1 \end{bmatrix} \tag{47}$$

is a 2-1-diagonal, known, tensor.

Finally, it remains to identify $\boldsymbol{F}_{\mathrm{p}}$ from the measured S and x. This is possible, by using the plastic incompressibility, $\det(\boldsymbol{F}_{\mathrm{p}}) = 1$ and the elastic law in Equation (30) assuming known elastic constants. A non-linear equation system must be solved. In conclusion, we can also in the case of a finite strain formulation use the proposed calibration strategy and investigation of the role of the accumulated plasticity λ.

References

Ahlström, J., Karlsson, B., 2005. Fatigue behaviour of rail steel - A comparison between strain and stress controlled loading. Wear 258, 1187–1193. doi:10.1016/j.wear.2004.03.030.

Bari, S., Hassan, T., 2002. An advancement in cyclic plasticity modeling for multiaxial ratcheting simulation. International Journal of Plasticity 18, 873–894. URL: http://www.sciencedirect.com/science/article/pii/S0749641901000122, doi:10.1016/S0749-6419(01)00012-2.

Bartels, A., Mosler, J., 2017. On the numerical implementation of thermomechanically coupled distortional hardening. International Journal of Plasticity 96, 182–209. doi:10.1016/J.IJPLAS.2017.05.003.

Barthel, C., Levkovitch, V., Svendsen, B., 2008. Modeling of sheet metal forming processes taking into account distortional hardening. International Journal of Material Forming 1, 105–108. doi:10.1007/s12289-008-0035-y.

Chaboche, J., 1986. Time-independent constitutive theories for cyclic plasticity. International Journal of Plasticity 2, 149–188. doi:10.1016/0749-6419(86)90010-0.

Chaboche, J.L., Van, K.D., Cordier, G., 1979. Modelization of the Strain Memory Effect on the Cyclic Hardening of 316 Stainless Steel. Technical Report. SMiRT 5. Berlin, Germany. URL: https://repository.lib.ncsu.edu/handle/1840.20/26854.

El Abdi, R., Samrout, H., Gambart, G., 1999. Elastoviscoplasticity with plastic strain memory. European Journal of Mechanics, A/Solids 18, 421–431. doi:10.1016/S0997-7538(99)00122-9.

EN10305-1, 2016. Steel tubes for precision applications - Technical delivery conditions - Part 1: Seamless cold drawn tubes.

EN13674-1, 2011. Railway applications - Track - Rail - Part 1: Vignole railway rails 46 kg/m and above. EUROPEAN COMMITTEE FOR STANDARDIZATION.

Feigenbaum, H.P., Dafalias, Y.F., 2007. Directional distortional hardening in metal plasticity within thermodynamics. International Journal of Solids and Structures 44, 7526–7542. URL: http://www.sciencedirect.com/science/article/pii/S0020768307002077, doi:10.1016/j.ijsolstr.2007.04.025.

Harrysson, M., Ristinmaa, M., 2007. Description of evolving anisotropy at large strains. Mechanics of Materials 39, 267–282. doi:10.1016/j.mechmat.2006.05.005.

Ishikawa, H., Sasaki, K., 1988. Yield Surfaces of SUS304 Under Cyclic Loading. Journal of Engineering Materials and Technology 110, 364–371. doi:10.1115/1.3226064.

Khan, A.S., Wang, X., 1993. An experimental study on subsequent yield surface after finite shear prestraining. International journal of plasticity 9, 889–905. doi:10.1016/0749-6419(93)90056-V.

Lemaitre, J., Chaboche, J.L., 1990. Mechanics of Solid Materials. Cambridge University Press, Cambridge. doi:10.1017/CBO9781139167970.

Lomer, W.M., 1952. The yield phenomenon in polycrystalline mild steel. Journal of the Mechanics and Physics of Solids 1. doi:10.1016/0022-5096(52)90007-0.

Meyer, K.A., Ekh, M., Ahlström, J., 2018. Modeling of kinematic hardening at large biaxial deformations in pearlitic rail steel. International Journal of Solids and Structures 130-131, 122–132. URL: https://doi.org/10.1016/j.ijsolstr.2017.10.007, doi:10.1016/j.ijsolstr.2017.10.007.

Meyer, K.A., Menzel, A., 2021. A distortional hardening model for finite plasticity. International Journal of Solids and Structures (in press) doi:https://doi.org/10.1016/j.ijsolstr.2021.111055.

Moreton, D.N., Moffat, D.G., Hornby, R.P., 1978. Techniques for investigating the yield surface behavior of pressure-vessel materials. Journal of Strain Analysis 13, 185–191.

Naghdi, P.M., Essenburg, F., Koff, W., 1958. An experimental study of initial and subsequent yield surfaces in plasticity. Journal of Applied Mechanics 25, 201–209.

Noman, M., Clausmeyer, T., Barthel, C., Svendsen, B., Huétink, J., van Riel, M., 2010. Experimental characterization and modeling of the hardening behavior of the sheet steel LH800. Materials Science and Engineering A 527, 2515–2526. doi:10.1016/j.msea.2009.12.013.

Novak, J.S., De Bona, F., Benasciutti, D., 2019. An isotropic model for cyclic plasticity calibrated on the whole shape of hardening/softening evolution curve. Metals 9. doi:10.3390/met9090950.

Park, T., Abu-Farha, F., Pourboghrat, F., 2019. An evolutionary yield function model based on plasticwork and non-associated flow rule. Metals 9. doi:10.3390/met9050611.

Phillips, A., Juh-Ling, T., 1972. The effect of loading path on the yield surface at elevated temperatures. International Journal of Solids and Structures 8, 463–474. doi:10.1016/0020-7683(72)90017-0.

Phillips, A., Liu, C.S., Justusson, J.W., 1972. An experimental investigation of yield surfaces at elevated temperatures. Acta Mechanica 14, 119–146. doi:10.1007/BF01184853.

Pietryga, M.P., Vladimirov, I.N., Reese, S., 2012. A finite deformation model for evolving flow anisotropy with distortional hardening including experimental validation. Mechanics of Materials 44, 163–173. doi:10.1016/j.mechmat.2011.07.014.

Qin, J., Holmedal, B., Hopperstad, O.S., 2018. A combined isotropic, kinematic and distortional hardening model for aluminum and steels under complex strain-path changes. International Journal of Plasticity 101, 156–169. URL: https://www.sciencedirect.com/science/article/pii/S0749641917302425?via%3Dihub, doi:10.1016/J.IJPLAS.2017.10.013.

Ristinmaa, M., Wallin, M., Ottosen, N.S., 2007. Thermodynamic format and heat generation of isotropic hardening plasticity. Acta Mechanica 194, 103–121. doi:10.1007/s00707-007-0448-6.

Shi, B., Bartels, A., Mosler, J., 2014. On the thermodynamically consistent modeling of distortional hardening: A novel generalized framework. International Journal of Plasticity 63, 170–182. doi:10.1016/j.ijplas.2014.05.008.

Sommer, C., Christ, H.J., Mughrabi, H., 1991. Non-linear elastic behaviour of the roller bearing steel SAE 52100 during cyclic loading. Acta Metallurgica et Materialia 39, 1177–1187. doi:10.1016/0956-7151(91)90206-G.

Sung, S.J., Liu, L.W., Hong, H.K., Wu, H.C., 2011. Evolution of yield surface in the 2D and 3D stress spaces. International Journal of Solids and Structures 48, 1054–1069. doi:10.1016/j.ijsolstr.2010.12.011.

Taleff, E.M., Lewandowski, J.J., Pourladian, B., 2002. Microstructure-property relationships in pearlitic eutectoid and hypereutectoid carbon steels. Jom 54, 25–30. doi:10.1007/BF02700982.

Wang, Y., Tomota, Y., Ohmura, T., Gong, W., Harjo, S., Tanaka, M., 2020. Continuous and discontinuous yielding behaviors in ferrite-cementite steels. Acta Materialia 196, 565–575. URL: https://doi.org/10.1016/j.actamat.2020.07.017, doi:10.1016/j.actamat.2020.07.017.

Zhou, J., Sun, Z., Kanouté, P., Retraint, D., 2018. Experimental analysis and constitutive modelling of cyclic behaviour of 316L steels including hardening/softening and strain range memory effect in LCF regime. International Journal of Plasticity 107, 54–78. doi:10.1016/j.ijplas.2018.03.013.